Journal of Pathology, Microbiology and Immunology

PMI
PATHOLOGY
MICROBIOLOGY
IMMUNOLOGY

ORIGINAL ARTICLE

Unraveling the Bifunctional HisIE Enzyme in *Acinetobacter baumannii* JJAB01: A Novel Therapeutic Target for Combating Antimicrobial Resistance

Raji Rajmichael[1] | Nagarajan Hemavathy[1] | Sangavi Pandi[2,3] | Saritha Poopandi[1] | Umashankar Vetrivel[4] | Jeyaraman Jeyakanthan[1]

[1]Structural Biology and Bio-Computing Lab, Department of Bioinformatics, Science Block, Alagappa University, Karaikudi, Tamil Nadu, India | [2]Department of Microbiology, Karpagam Academy of Higher Education, Coimbatore, Tamil Nadu, India | [3]Center for Bioinformatics, Karpagam Academy of Higher Education, Coimbatore, Tamil Nadu, India | [4]Virology & Biotechnology/Bioinformatics Division, ICMR-National Institute for Research in Tuberculosis, Chennai, Tamil Nadu, India

Correspondence: Jeyaraman Jeyakanthan (jjbioinformatics@gmail.com)

Received: 26 May 2025 | **Revised:** 26 August 2025 | **Accepted:** 9 September 2025

Funding: R.R. acknowledges the Indian Council of Medical Research, New Delhi (ICMR) for providing financial assistance through the ICMR/SRF Fellowship (AMR/Fellowship/24/2022-ECD-II).

Keywords: antimicrobial resistance | high-throughput virtual screening | HisIE inhibition | homology modeling | molecular dynamics simulation | structure-based drug design

ABSTRACT

Antimicrobial resistance (AMR) in ESKAPE pathogens presents a critical global health challenge, particularly in hospitals. The enzyme HisIE from *A. baumannii* was explored as a therapeutic target using structure-based drug design to combat bacterial infections. This study integrates various computational approaches, including homology modeling, molecular dynamics simulations (MDS), and structure-based virtual screening to identify the potent inhibitors with high binding affinity and favorable pharmacokinetic properties. High-throughput virtual screening of the COCONUT database identified lead compounds featuring strong binding affinities to protein targets along with favorable pharmacokinetic profiles. CNP0007442, CNP0007145, and CNP0007506 emerged as the most potent candidates based on MM/GBSA binding free energy calculations. They exhibited stable interactions with key active site residues (His98) of *Ab*HisIE, primarily through Van der Waals and electrostatic forces, enabling enhanced enzyme inhibition. Furthermore, density functional theory analysis revealed optimal HOMO–LUMO energy gaps, indicating the selected compounds' potential reactivity and stability. The findings highlight these candidates for further experimental validation, offering a novel therapeutic approach by disrupting the essential bacterial metabolic pathways. This study identifies promising drug-like molecules targeting *Ab*HisIE, offering a novel strategy to combat AMR infections.

1 | Introduction

Acinetobacter baumannii is a Gram-negative coccobacillus responsible for severe healthcare and community-associated infections [1]. This is one among the members of ESKAPE Pathogens (*Enterococcus faecium, Staphylococcus aureus, Klebsiella pneumoniae, A. baumannii, Pseudomonas aeruginosa*, and *Enterobacter spp*) as referred to by the Infectious Disease Society of America (IDSA) [2]. Over the past 3 decades, *A. baumannii* has emerged as a formidable pathogen in clinical settings, primarily due to its rapid development of antibiotic resistance [3]. ESKAPE pathogens exhibit a high capacity to acquire resistance through strategies such as drug inactivation, alteration of the drug binding pocket, and diminished drug uptake, and redefining key concepts in their pathogenesis, transmission, and treatment options [4, 5]. *A. baumannii* is potent in causing a broad

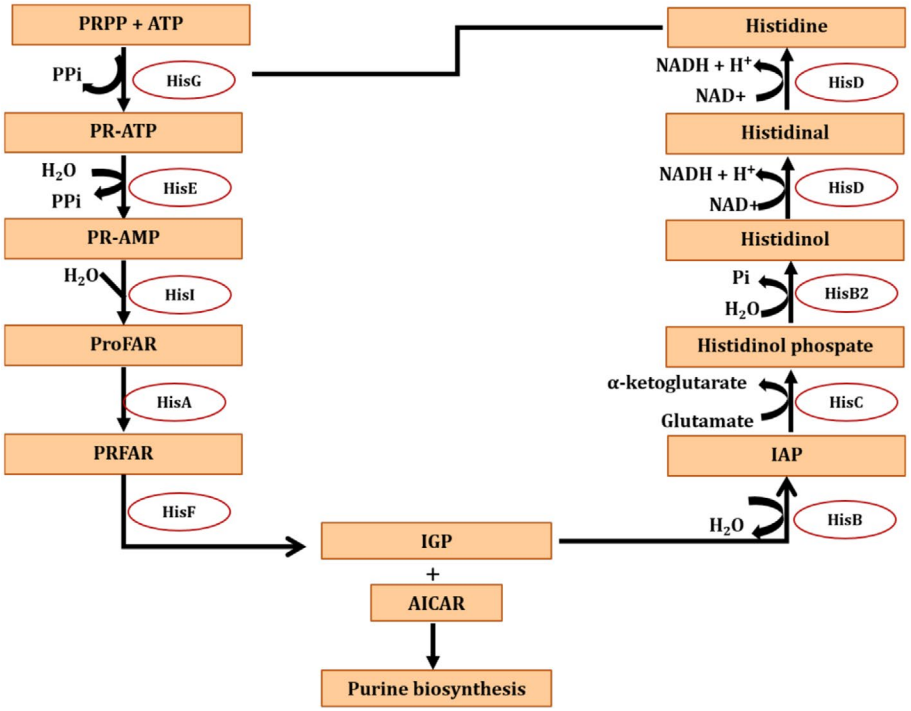

FIGURE 1 | Schematic representation of the histidine biosynthesis pathway, illustrating the sequential enzymatic reactions from phosphoribosyl pyrophosphate (PRPP) to histidine.

spectrum of infections, like pneumonia, meningitis, urinary tract infections, and tissue and skin infections in both hospital and community settings [6]. Risk factors such as prolonged hospital stays, immunosuppression conditions, age, trauma, prior antibiotic treatment, and invasive medical procedures, including surgeries, catheter insertions, or mechanical ventilation, contribute to hospital-acquired infections, especially in critically ill patients [7, 8]. This has resulted in increased instances of *A. baumannii* isolates exhibiting multiple drug resistance (MDR), extensive drug resistance (XDR), and pan-drug resistance (PDR) globally [9, 10]. Eastern and Southern Europe, Latin America, and several Asian countries have been reported to have high rates of antimicrobial resistance [3].

Carbapenems such as imipenem, meropenem, ertapenem, doripenem, and biapenem, while newer additions such as razupenem, tebipenem, tomopenem, and sanfetrinem were considered common treatment options for various bacterial infections due to their broad spectrum of antibacterial activity and improved resistance to most β-lactamases [11]. Carbapenem resistance can arise through several mechanisms, including the action of specific hydrolytic enzymes such as Class A β-lactamases, Class B metallo-β-lactamases, Class D β-lactamases, as well as down-regulation of porins in the bacterial outer membrane, which enhances resistance [12, 13]. Carbapenem-resistant *Acinetobacter baumannii* (CRAb) is recognized as the top critical priority pathogen by the World Health Organization (WHO). Moreover, the Centers for Disease Control and Prevention (CDC) has recognized this as a vital public concern, emphasizing the need to develop new therapeutic approaches [14, 15]. In the absence of an effective strategy to combat AMR, up to 10 million lives could be lost by 2050. Also, a socioeconomic burden exists due to the rising economic impact of AMR [16]. The COVID-19 pandemic had a profound effect on the landscape of secondary infections caused by MDR pathogens, notably CRAb, thus elevating the high mortality rate [17–19]. CRAb is frequently linked with the production of acquired carbapenemases, with Class D β-lactamases, also known as OXAs, being most prevalent [20, 21]. With the increasing CRAb, polymyxins and tigecycline have emerged as a second-line treatment option. However, the rise of polymyxin resistance has also been reported [22]. Despite multiple efforts, AMR still exists as a serious public health concern, emphasizing the urgent need to develop new antibiotics and alternative therapies to address this issue.

The histidine biosynthesis pathway (HBP) is an essential metabolic pathway involving 11 enzymatic reactions catalyzed by enzymes such as HisG, HisE, HisI, HisA, HisF, HisB, HisC, and HisD, with intermediate metabolites such as phosphoribosyl-ATP (PR-ATP), phosphoribosyl-AMP (PR-AMP), phosphoribosylformimino-AICAR-phosphate (ProFAR), phosphoribulosylformimino-AICAR-phosphate (PRFAR), imidazole glycerol phosphate (IGP), and imidazole acetol phosphate (IAP). This pathway also highlights the link between histidine and purine biosynthesis (Figure 1). The HisG protein catalyzes the initial step involving the displacement of the C-1 phosphoribosyl pyrophosphate (PRPP) by the N-1 nitrogen of adenosine triphosphate (ATP) purine ring, facilitated by a Mg^{2+} ion. This condensation reaction releases a pyrophosphate molecule, flips the ribose moiety from its α- to β-configuration, and, although reversible, is inhibited by the accumulation of L-histidine through product feedback inhibition. This regulation by feedback inhibition plays a critical role in adapting the flow of intermediates through the histidine biosynthesis pathway. Subsequent steps include the irreversible, Mg^{2+}-dependent hydrolysis of N′-5-phosphoribosyl-ATP to form N′-5-phosphoribosyl-AMP and pyrophosphate, a reaction catalyzed by the carboxy-terminal domain of the HisI enzyme. Then, it is followed by a ring-opening

reaction, mediated by HisI, in the pathway. HisIE exhibits in a dimer form in *E. coli* and *S. typhimurium*, requiring Zn^{2+} and Mg^{2+} ions for activity, although Zn^{2+} can be substituted by Cd^{2+}, resulting in altered catalytic properties. The dimer interface forms the active site pocket for binding the substrate phosphoribosyl-AMP (PR-AMP) cyclohydrolase and Zn^{2+}. This enzyme consists of an N-terminal domain, HisI, and a C-terminal domain, HisE, connected by a fusion loop. The C-terminal HisE-like domain is thought to catalyze the Mg^{2+}-dependent hydrolysis of PR-ATP to N1-(5-phospho-β-D-ribosyl)-AMP (PR-AMP) and pyrophosphate (PPi). The N-terminal HisI-like domain to mediate the Zn^{2+} dependent ring-opening hydrolysis of PR-AMP, producing N-(5′-phospho-D-ribosylformimino)-5-amino-1-(5″-phospho-D-ribosyl)-4-imidazolecarboxamide (ProFAR) [23].

The HBP is highly conserved in Gram-negative bacteria, representing a prime focus for antibiotic development. However, gene fusion within this pathway is a common evolutionary adaptive strategy that confers a selective advantage in pathogenic bacteria [24]. The lack of structural information limits our understanding of the domain organization and catalytic functions of these fusion enzymes. However, structural studies could provide insights into the molecular mechanisms underlying gene fusion and elongation [25, 26]. Studies in *A. baumannii* revealed that these essential enzymes in the histidine biosynthesis pathway, including HisIE, are critical for bacterial persistence in the lungs during pneumonia infection. This finding underscores the pathway's role in *A. baumannii's* survival and virulence in the host respiratory tract [27]. Moreover, histidine plays a crucial role in zinc acquisition and the establishment of lung infections by *A. baumannii*, making enzymes of this pathway attractive drug candidates due to their essential functions during infection and lack of homologs in humans [24, 28–32].

In this study, HisIE, a bifunctional enzyme from *A. baumannii* JJA01 [33] was chosen as a drug target, and its dimer model was generated using homology modeling. Furthermore, chain and domain-based comparative molecular dynamics simulations were employed to assess the tertiary structural stability of *Ab*HisIE. Structure-based virtual screening was performed on the active site pocket of the target protein to identify probable drug-like candidates. Additionally, density functional theory (DFT) calculations and ADME/T analysis were used to assess the lead's reactivity. This *in silico* technique utilized the active site pocket of *Ab*HisIE to identify the reactivity and pharmacokinetic properties of the lead compounds. This approach facilitates the identification of novel inhibitors targeting *Ab*HisIE, contributing to the development of effective therapies against AMR infections.

2 | Materials and Methodology

2.1 | Sequence Analysis and Structure Prediction

*Ab*HisIE amino acid sequence was retrieved from the NCBI database (accession number: WP_001066569.1). The physicochemical parameters were evaluated using the ExPASy server [34]. The secondary structure properties of the target protein were assessed through the Self-Optimized Prediction Method with Alignment (SOPMA) [35]. The NCBI BLASTp search was performed against the Protein Data Bank (PDB) to identify homologous structures [36]. Based on the selected templates, homology modeling was performed using Modeler 10 V4 to model the three-dimensional model of the *Ab*HisIE protein. From the generated models, the lowest discrete optimized protein energy (DOPE) score was chosen for refinement using the Protein Preparation Wizard in the Schrodinger suite. Furthermore, the quality of the refined model was determined using PROCHECK and ProSA [37, 38].

2.2 | Molecular Dynamics Simulation

Molecular dynamics simulations (MD) were performed on the *apo* form of modeled *Ab*HisIE and the *Ab*HisIE-top compounds complexes retrieved from HTVS, using GROMACS version 2019 to investigate the structure–function relationships of proteins and protein–ligand complexes. The topology for the protein was generated with the pdb2gmx module using the CHARMM36 force field. While the topology for the ligand was generated through the CHARMM General Force Field (CGenFF) server [39]. The solvation of the protein–ligand complex significantly influences its structural properties and dimensions. Subsequently, periodic boundary conditions (PBC) simulate a more extensive system, with a unit cell replicated in all spatial directions. The simulation operates solely within the confines of the PBC box; any erroneous connections are rectified by executing a brief energy minimization. Na^{+} and Cl^{-} ions were incorporated to maintain overall neutrality, followed by energy minimization using the steepest descent algorithm [40]. The system was equilibrated at a temperature of 310 K for a duration of 5000 steps, corresponding to 10 ps (ps). Each system underwent equilibration using either an isothermal-isobaric (NPT) ensemble, which maintains constant particle number, pressure, and temperature, or an isothermal-isochoric (NVT) ensemble, characterized by a constant number of particles, volume, and temperature. The LINCS algorithm was employed to constrain hydrogen bonds with a time step of 2 femtoseconds (fs). Following these preparations, a production simulation lasting 200 ns was conducted. Henceforth, the trajectory files were examined using GROMACS tools to explore the complex's dynamic conformational changes and interactions over time [41]. The gmx_rms module accurately calculated the root mean square deviation (RMSD). Additionally, the gmx_rmsf function facilitated the computation of root mean square fluctuations (RMSF) based on the C-alpha atoms of the protein. The gmx_gyrate tool was utilized to assess the gyration radius of each protein atom. At the same time, the gmx_hbond function was applied to quantify the number of hydrogen bonds present at the protein–ligand interface.

2.3 | Active Site Prediction

Previous studies have reported that the substrate PR-AMP cyclohydrolase binds within the active site pocket of *Ab*HisIE, which is formed by 18 key residues, 16 of which are functionally conserved. The catalytic mechanism is further enhanced by Zn^{2+} and Mg^{2+} ions [42, 43]. The structural mapping of the *Ab*HisIE active site was determined by identifying homologs

from the protein data bank (PDB) through a BLASTp search. Superimposing the homologous structures revealed well-conserved active site pockets and overall structural folds. Additionally, multiple sequence alignment (MSA) using ClustalW [44] was performed to pinpoint conserved residues for subsequent docking analyses.

2.4 | Molecular Docking

The substrate PR-AMP cyclohydrolase (ID: 440154) was obtained from the PubChem database and prepared using the LigPrep module of Schrodinger Release 2023-1 from LLC, NY. Following this, the receptor grid was generated based on the predicted active site residues [45]. Furthermore, molecular docking was conducted using Extra Precision mode (XP) to evaluate the substrate's binding potential.

2.5 | Ligand Preparation and Structure-Based Virtual Screening

An extensive collection of natural product catalogs called the COlleCtion of Open Natural prodUcTs (COCONUT) database was employed for the streamlined virtual screening process. COCONUT offers greater chemical diversity and more detailed structural annotations, thereby enhancing opportunities for identifying novel scaffolds with drug-like properties. In addition, it includes critical stereochemical and physicochemical data, making it particularly well-suited for structure-based virtual screening approaches such as molecular docking and pharmacophore mapping. These features make the COCONUT database an ideal resource for the present study, which focuses on discovering natural product-derived inhibitors of the target enzyme. All these compounds from the database were prepared using the LigPrep module within the Schrödinger suite (LigPrep, Schrödinger LLC, New York, NY, 2023-1). The optimized ligand datasets were then subjected to structure-based virtual screening against the active site of *Ab*HisIE. This process involved filtering compounds through the GLIDE module in three phases: High-throughput virtual screening (HTVS), standard precision (SP), and extra precision (XP) modes [46]. We retained the top 10% of compounds with optimal docking and highest-scoring states. The SP docking score identified ligands with a strong propensity to interact with the *Ab*HisIE binding pocket. Simultaneously, the XP scoring function filters out false positives with inadequate pharmacokinetic properties. The top compounds were selected for further computational analysis following the successful high-throughput multiscale screening via SP and XP modes.

2.6 | ADME/T Prediction

The screened compounds from HTVS were assessed for their absorption, distribution, metabolism, and excretion (ADME) properties using the Qikprop module within Schrödinger Release 2023-1 LLC, NY. The drug-likeness and pharmacokinetic properties, adhering to Lipinski's rule of five, which includes criteria such as a molecular weight below 500, <5 hydrogen bond donors, <10 hydrogen bond acceptors, and a log p value <5, were checked. Moreover, the apparent MDCK cell permeability (QPP MDCK), apparent CaCo-2 permeability (QPP Caco), blood–brain partition coefficient (QPlog BB), octanol/gas partition coefficient (QPlog PO/w), octanol/water partition coefficient (QPlog PO/w), water/gas partition coefficient (QPlogPW), and aqueous solubility (QPlogs) were evaluated to identify the drug-likeness of the selected leads. Moreover, evaluating potential toxicity concerns for the top compounds is essential to ensure a comprehensive drug safety assessment. Using computational predictions, key toxicity risks such as hepatotoxicity, cardiotoxicity, and off-target interactions should be addressed. By integrating the toxicity profile, we can prioritize compounds with optimal efficacy–safety balances, reducing attrition in later stages of drug development. The toxicity profiles of the chosen leads were assessed in the ToxinPred Server using their canonical simplified molecular-input line-entry system (SMILES) [47]. A score below 0.5 indicates that the compound exhibits nontoxic behavior.

2.7 | MM/GBSA Analysis

The binding free energy for the top-hit compounds was calculated based on the high docking scores and molecular interactions. The binding energy is the summation of the intermolecular interactions between the ligand and the protein, as well as the steric energy of the ligand. This analysis used the Prime molecular mechanics general born surface area (MM/GBSA) method, Schrodinger Release 2023-1 LLC, NY [48]. The study aimed to refine the search for the potential compounds based on the free-binding energy of their respective complexes. The binding energy was calculated using the following equation: $\Delta G_{binding} = \Delta G_{complex} - [\Delta G_{protein} + \Delta G_{ligand}]$.

2.8 | Density Functional Theory

The Jaguar module of Schrödinger was employed to conduct density functional theory (DFT) computations. The DFT approach is utilized to ascertain single point energy (SPE), which reflects the electronic characteristics, and to examine the attributes of each compound's atomic structure, electronic properties, and energy states [49]. The electronic properties of the lead compounds were evaluated using the Jaguar module from Schrödinger (Schrodinger Release 2023-1 LLC, NY). A 6-31G*$^{++}$ basis set was implemented to perform comprehensive geometry optimization using the Hybrid DFT model, incorporating Becke's three-parameter exchange potential alongside the correlation functional of Lee, Yang, and Parr. The energy calculations utilized the Adaptive Poisson–Boltzmann Finite (PBF) solvation method within physiological conditions. This methodology is employed to determine the energies of the highest occupied molecular orbital (HOMO) and the lowest unoccupied molecular orbital (LUMO). The HOMO represents the orbital with the highest energy and is characterized as electron-rich, possessing the capacity to donate electrons. Conversely, the LUMO is the lowest energy orbital that remains vacant, indicating its ability to accept electrons. A reduced energy gap between the HOMO and LUMO plays a crucial role in influencing the bioactivity and intermolecular

charge transfer of molecular structures. The energy difference between the HOMO and LUMO, defined as the HOMO–LUMO energy gap (ΔE), provides insights into the electronic properties, potential bioactivity, reactivity, and kinetic stability of small molecules. Lower ΔE signifies intensified reactivity, fostering more substantial and advantageous interactions with the target enzyme through charge transfer or orbital overlap mechanisms. Conversely, an excessively high energy gap suggests chemical inertness, which may hinder binding efficiency.

2.9 | MM/PBSA Analysis

The molecular mechanics Poisson–Boltzmann surface area (MM/PBSA) technique determined the binding free energy between the protein and ligand. This approach calculates binding free energy by integrating thermodynamic cycles and molecular dynamics (MD) methodologies [50]. The change in binding free energy is evaluated by comparing various energy components, including van der Waals forces, electrostatic interactions, and solvation energies. The binding free energy calculations were conducted on trajectories taken at 50 ns intervals from 200 ns MDS trajectories. The MM/PBSA assessments for the protein–ligand complexes were performed using the gmx_MMPBSA function within the GROMACS software package [51]. Furthermore, the Python tool MMPBSA.py was employed to calculate the binding free energy (ΔG_bind).

3 | Results and Discussion

3.1 | Sequence Analysis and Structure Prediction

The *Ab*HisIE enzyme, composed of 257 amino acids with 27 positively charged residues (Arg + Lys) and 37 negatively charged residues (Asp + Glu), has a molecular mass of 29.14 kDa, an isoelectric point of 6.65, an aliphatic index of 35.52, and a grand average of hydropathicity (GRAVY) of −0.488. The secondary structure comprised 40.47% α-helix, 12.45% β-strand, and 47.08% random coil. The dimeric protein exhibited a well-organized secondary structure featuring 8 α-helices, 6 β-strands, and 2 β-sheets, providing structural stability (Figure S1). Overall, it was observed to facilitate the structural folding and flexibility for enhanced substrate binding and catalytic activity. For three-dimensional structure modeling, the template PDB ID: 6J2L was chosen based on sequence identity of 36.12%, a maximum of 88% query coverage, and the lowest E-value of 2e−35. Mg^{2+} and Zn^{2+} metal ions were incorporated into the three-dimensional model of *Ab*HisIE. The predicted *Ab*HisIE (Figure 2) with the lowest DOPE score demonstrated 81.2% of residues in the favored region, 16.2% in the additionally allowed region, and 0.9% in the disallowed region of the Ramachandran Plot. The structural superimposition of *Ab*HisIE with the template showed an RMSD of 0.15 Å, thus validating the accuracy of the predicted model, which was subsequently used for further studies (Figures S2 and S3). Dimeric Fusion *Ab*HisIE protein comprises two catalytic domains (HisI: Gln5-Tyr106 and HisE: Val146-Arg242) and a dimeric loop (DL: Arg107-Gln145) segment as a linker between the two domains. The bifunctionality

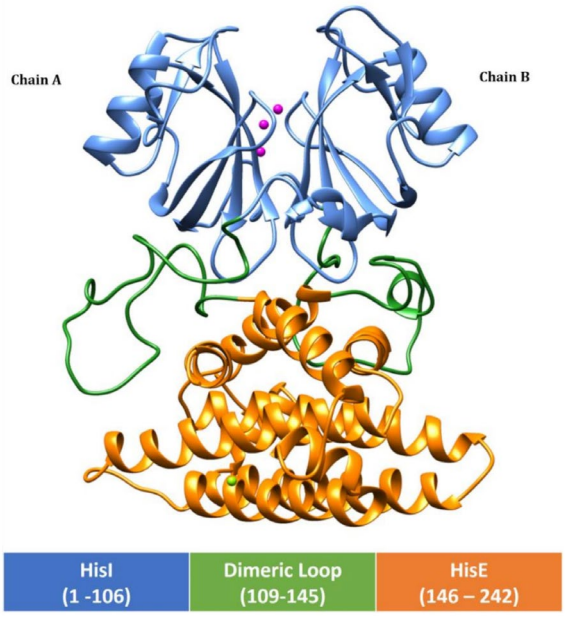

FIGURE 2 | Modeled dimeric structure of *Ab*HisIE: HisI (5–106), Dimeric Loop (107–145), and HisE (146–242) in complex with Mg^{2+} and Zn^{2+} ions were shown as Green and magenta Sphere, respectively.

of HisI and HisE enhances the substrate binding and increases the catalytic efficacy of histidine biosynthesis.

3.2 | Dimeric Apo MD Analysis

The overall RMSD profiling analysis of dimeric *Ab*HisIE (Chains A and B) shows that Chain B had a higher RMS deviation than Chain A. Initially, both chains exhibited high RMS deviations of ~1.5 nm at 60 ns; however, the system continued to equilibrate until the end of the MD production run. The average RMSD values were 1.28 nm for Chain A and 1.54 nm for Chain B, with standard deviations of 0.41 nm and 0.44 nm, respectively. A comparative domain-based RMSD analysis indicated that the HisI and HisE domains of Chain A and Chain B exhibited minimal deviations. In contrast, the higher RMS deviations were only observed in the dimeric loop region of both Chain A and Chain B, which predominantly adopt a loop conformation with RMS deviations of 1.3 and 1.4 nm, respectively. This infers that the higher RMS deviations of the monomeric Chains are predominantly due to the higher deviations of their respective dimeric segment.

The RMSF analysis revealed distinct fluctuation patterns in Chains A and B. In Chain A, within the HisE region, Asn216 showed the least fluctuation at 0.22 nm. In contrast, Glu163 and Ala200 exhibited significant fluctuations of ~1.4 nm. Within the HisI region, Ala140 demonstrated the highest fluctuation with an RMSF value of 1.48 nm. For Chain B, Tyr128, Glu135, Gln161, Glu163, and Asp165 had high fluctuations around 1.3 nm. Notably, Glu163 was a common residue with high fluctuations in both chains, while Asp216 in Chain A and Chain B residues, namely, Thr214 and Leu217, were observed to have the least fluctuations. These results highlight the two chains' shared and unique dynamic behaviors (Figure 3a–d).

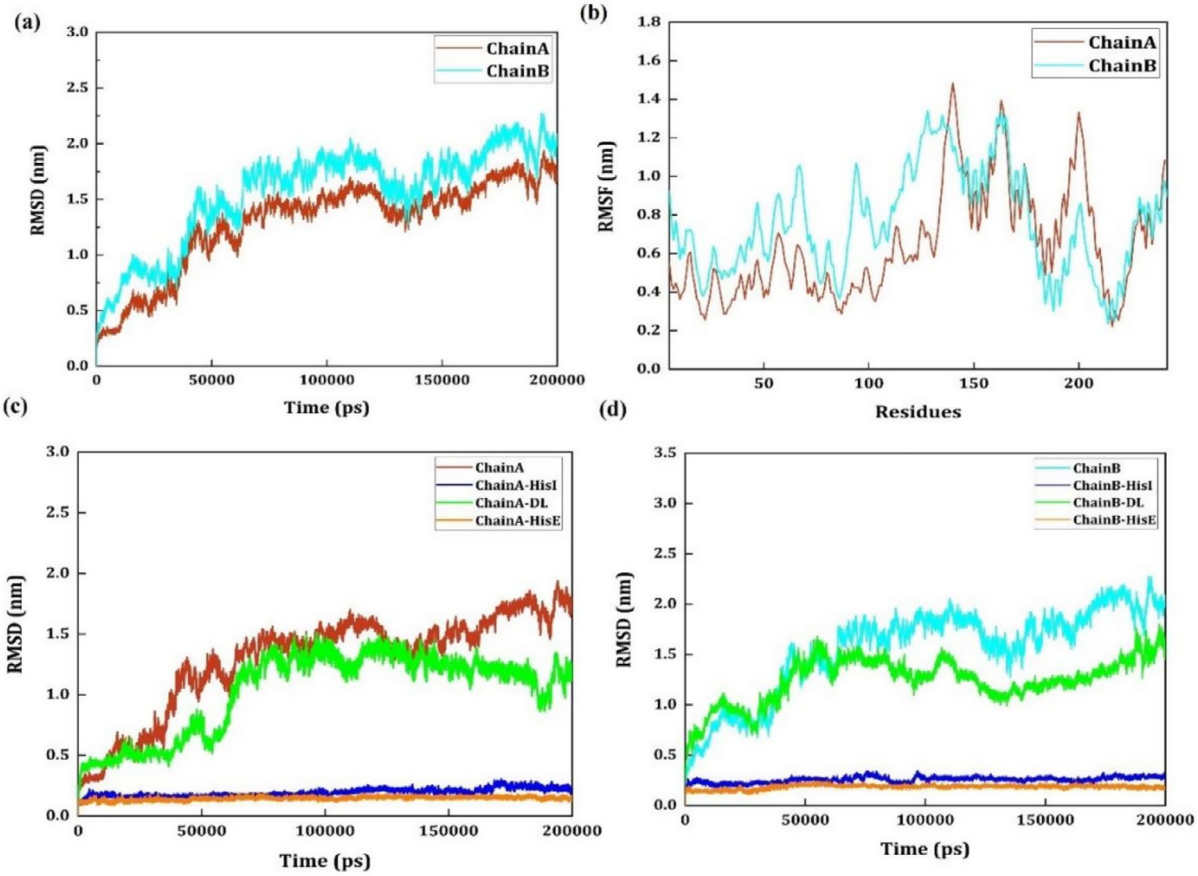

FIGURE 3 | Molecular dynamics simulation analysis of the dimeric *Ab*HisIE: Chain A (brown), Chain B (cyan), HisI (Blue), DL (Green), and HisE (orange) (a) Comparative RMSD analysis of Chain A and Chain B, (b) RMSF analysis of Chain A and Chain B, Domain-based comparative RMSD analysis of (c) Chain A and (d) Chain B.

3.3 | Multiple Sequence Alignment and Active Site Identification

Two primary structural homologs were selected based on query coverage and identity: 6J2L (88%) from *Shigella flexneri* and 1ZPS (46%) from *Methanobacterium thermoautotrophicum* [43, 45]. The Multiple Sequence Alignment of *Acinetobacter baumannii* HisIE (WP_001066569.1), *Methanobacterium thermoautotrophicum* HisI (PDB ID: 1ZPS), and HisIE *S. flexneri* (PDB ID: 6J2L) highlights the conserved residues such as Leu18, Gln23, Gly28, Leu31, Met32, Met36, Asn37, Glu39, Leu41, Thr44, Glu46, Ser54, Leu60, Trp61, Lys63, Gly64, Glu65, Ser67, Gly68, Val73, Asp79, Cys80, Asp81, Asp83, Gly93, Cys98, His99, Gly100, Ser103, Cys104, Phe105, Asp123, Pro124, and Tyr128 within the *Ab*HisIE domain, represented in red. Additionally, the semi-conserved residues, namely, Ile/Met19, Ala/Val20, Ile/Val21, Ala/Val22, Thr/Ser27, Ile/Val30, Val/Leu33, Trp/Tyr35, Ala/Leu/Ile45, Ala/Val50, Tyr/Phe52, Phe/Trp53, Ser/Thr56, Arg/Lys57, Lys/Arg59, Ile/Val76, Ile/Val/Leu86, Val/Leu87, Leu/Val88, Val/Ala90, and Leu/Ile110 were represented in a red box (Figure S4). Since *Sf*HisIE is the first reported bifunctional enzyme, its substrate-binding pattern is highly conserved across species. To further investigate this, the putative substrate-binding site of *Sf*HisIE was superimposed with *Ab*HisIE. This analysis revealed key residues involved in substrate interaction, including Ser54, Trp61, Lys65, Glu66, Ser67, Cys97, His98, and Cys104 in Monomer A, as well as Glu14 and Asp83 in Monomer B. Additionally, the Zn^{2+} binding motif comprises Cys80, Cys96, and Cys104, while the Mg^{2+} binding motif includes Asp79, Asp81, and Asp83.

3.4 | Molecular Docking and Molecular Dynamics Simulation of HisIE With Substrate

The docking analysis for the Substrate PR-AMP cyclohydrolase reveals a highly favorable interaction with the target protein, as indicated by a strong docking score of −14.326 kcal/mol, suggesting a significant binding affinity. The Glide Energy, estimated at −95.484 kcal/mol, further substantiates this finding by demonstrating the complex formation's stability and energetically favorable nature. Additionally, the Glide Emodel score of −133.646 offers a comprehensive evaluation of the docking pose, reinforcing the conclusion of a highly favorable interaction. The calculated binding free energy (ΔG Bind) of −56.42 kcal/mol emphasizes the spontaneity and strength of the binding, signifying that the interaction is thermodynamically favorable. PR-AMP cyclohydrolase interacts with the specific residues on the protein, including Glu14, Val33, Ser54, Arg55, Gly64, Asp83, Ala96, and His98, which are likely involved in direct binding through hydrogen bond interactions. Additionally, the residues Lys63, Asp79, and Asp83 contribute to stabilizing the compound within the binding site through salt bridge interactions. His98 also plays

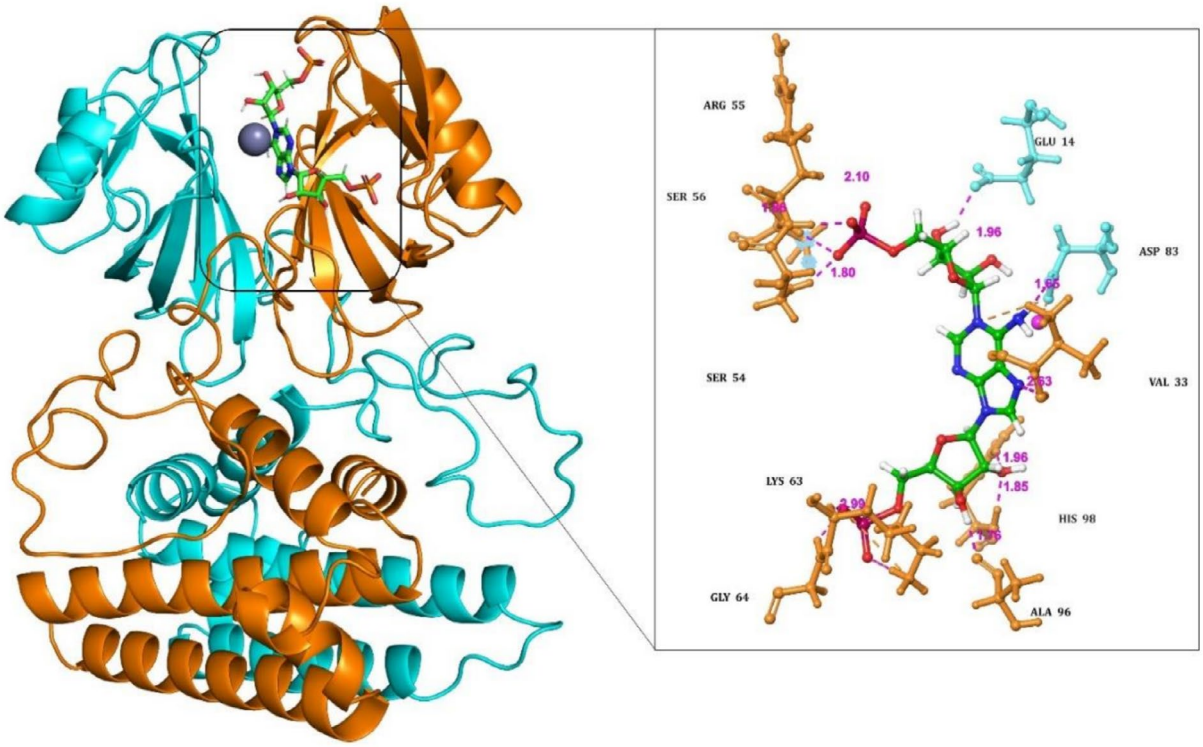

FIGURE 4 | Substrate binding at the HisIE active site pocket, highlighting the active site region and $Zn2^{+}$ ions (sphere). The inset figure shows the three-dimensional interaction of the substrate with HisIE.

a role in these interactions, reinforcing the compound's binding stability. These interactions provide crucial insights into the molecular basis of ligand binding, which could be instrumental in optimizing the compound for enhanced affinity and specificity or in elucidating its precise mechanism of action (Figure 4).

The structural stability of the HisIE_Substrate complex was further analyzed through MD simulations. RMSD analysis showed that the average RMSD was 0.52 nm for Chain A and 0.7 nm for Chain B, exhibiting fluctuations during the simulation. Chain A stabilized around 0.5–0.6 nm after 150 ns, while Chain B reached its maximum deviation of approximately 0.75 nm. However, Chain B remained stable from 75 ns throughout the simulation. Overall, Chain B demonstrated greater stability than Chain A, showing less deviation throughout the simulation (Figure 5a). The RMSF plot indicated the residual mobility and flexibility of Chain A and Chain B in the presence of the substrate. Both chains displayed significant fluctuations in the dimeric loop region, specifically residues Gln120 and Ala140. Although flexible loop regions typically exhibit more significant fluctuations, these variations do not destabilize the overall stability of the complex (Figure 5b). The key interacting residues from the HisI region identified within the complex include Val33 (0.09 nm), His98 (0.16 nm), Ser55 (0.15 nm), Ser56 (0.19 nm), and Arg57 (0.19 nm) from Chain A, alongside Glu14 (0.18 nm), Asp79 (0.12 nm), and Asp83 (0.10 nm) from Chain B. The minimal fluctuations observed in these residues suggest high structural stability within the complex (Figure 5b). The Rg plot provides insights into the compactness of the HisIE complex over time. Chain A exhibited a higher Rg value (around 2.40–2.50 nm) than Chain B (~2.30–2.40 nm) (Figure 5c). This suggests that Chain A adopts a slightly more extended conformation, while Chain B displays a gradual increase in compactness throughout the simulation. These results indicate that Chain B is more stable and compact, whereas Chain A retains structural flexibility and a dynamic nature.

Hydrogen bond interactions are crucial for maintaining the structural stability of the complex. Key hydrogen bond formations indicate that both chains, Chain A and Chain B, remain stable when interacting with the substrate. During the simulation, Chain A exhibited 5–6 hydrogen bond interactions, while Chain B maintained 4–5 hydrogen bonds, contributing to the overall stability of the complex throughout the simulation period (Figure 5d). Overall, insights from the MD simulation further revealed the structural stability and compactness of Chains A and B. Increased hydrogen bond interactions and reduced fluctuations of key residues reinforced this stability. These findings provide a deeper understanding of the molecular interactions between HisIE and the substrate, offering valuable insights for future studies on ligand binding and enzyme dynamics.

3.5 | Molecular Orbital Analysis of the Substrate

Figure 6 illustrates the Frontier molecular orbital of the substrate, as determined by its HOMO, LUMO, and energy gap value. The value of HOMO is −0.2087 eV, with the orbital density predominantly focused on the left-side moiety, indicating the presence of an electron-rich region that possesses a significant capacity for electron donation. Conversely, the

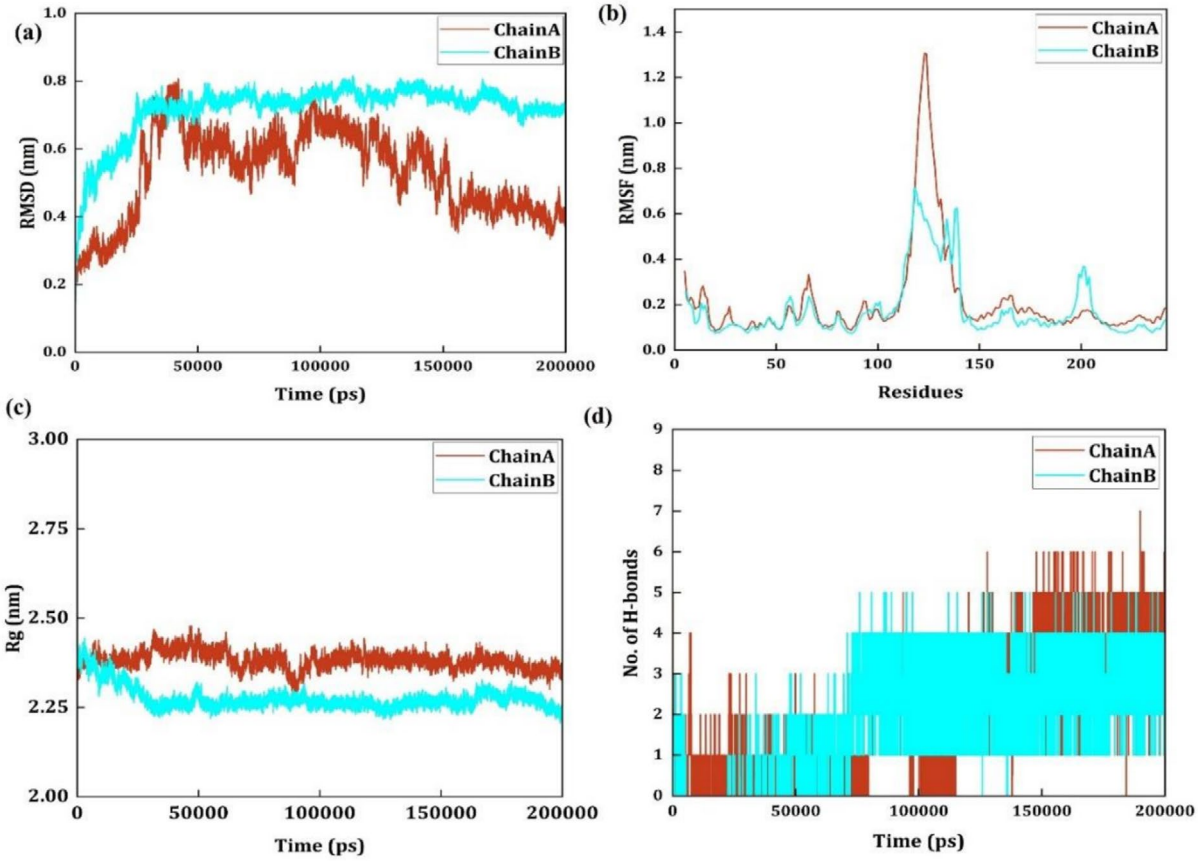

FIGURE 5 | Molecular dynamics simulation analysis of the dimeric HisIE with substrate PR-AMP, (a) comparative RMSD analysis of Chain A and Chain B, (b) RMSF analysis of Chain A and Chain B, (c) radius of gyration in both Chain A and B, and (d) H-bond interaction in Chain A and B.

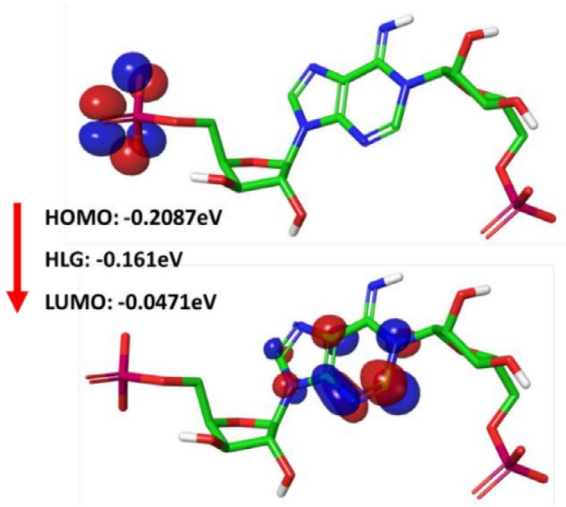

FIGURE 6 | Frontier molecular orbital (HOMO and LUMO) distributions along with their corresponding energy values (eV) of the substrate.

LUMO value is −0.0471 eV, exhibits orbital density concentrated around the core heteroaromatic ring and the right-side substituents, signifying electron-deficient regions conducive to electron acceptance. The obtained HOMO–LUMO energy gap of −0.1616 eV suggests favorable electronic polarizability, minimal excitation energy requirements, and enhanced potential for charge transfer.

3.6 | High-Throughput Virtual Screening

High-throughput virtual screening is used to screen the extensive libraries of drug-like compounds. A hierarchical high-throughput virtual screening approach with HTVS, standard precision (SP), and extra precision (XP) docking was employed to identify a potent inhibitor that binds in the active site pocket of the dimeric HisIE target protein. Initially, 407,246 compounds from the COCONUT database were subjected to HTVS mode (50%), and a further 50% of the compounds surpassed from HTVS were subjected to SP (30%). Finally, 119 compounds out of 1196 (10%) successfully passed the XP docking screening. The top five potential drug-like lead compounds were selected from an initial set of 10 candidates based on their glide score, energy, interaction residues, pharmacokinetics, and ADME/T properties (Figure S5 and Table 1).

3.7 | ADME/T Prediction

In silico predictions of ADME/T (absorption, distribution, metabolism, excretion, and toxicity) properties are crucial for anticipating the biological impact of identified lead compounds before starting in vitro studies. The results related to

drug-likeness and ADME/T indicate that all pharmacokinetic properties of the lead compounds fall within an acceptable range, qualifying them as drug-like molecules. Among the compounds evaluated, CNP0007442 exhibited the highest permeability (16.014), while CNP0007146 showed the lowest permeability (12.193), indicating a moderate variation in water permeability among the compounds. In terms of lipophilicity, CNP0007146 had the highest LogP value (4.787), suggesting greater lipid solubility, whereas CNP0007506 had the lowest LogP (3.314), indicating relatively lower lipid solubility. When considering solubility, CNP0007506 exhibited the highest solubility (−4.171), while CNP0007146 and CNP0007188 had the lowest solubility values (−5.540 and −5.497, respectively), which are essential for assessing aqueous solubility and potential drug absorption. CNP0007145 exhibits moderate aqueous solubility (−4.836) and the capacity to traverse the blood–brain barrier (QPP MDCK = 473.503). The potential for cardiac toxicity was evaluated by examining the inhibition of the hERG potassium channel. CNP0007146 presented the highest risk of hERG inhibition (−7.559), whereas CNP0007506 had the lowest risk (−5.022). Additionally, CNP0007146 had the highest permeability in a different context (611.215), while CNP0007442 showed the lowest permeability (186.696), indicating significant differences in absorption potential (Table 2).

3.8 | MM/GBSA Analysis

CNP0007442 exhibited the most substantial Coulomb interaction at −23.797 kcal/mol, indicating a stronger electrostatic attraction. In contrast, CNP0007146 had the weakest Coulomb interaction at −14.186 kcal/mol. Regarding Van der Waals energy, CNP0007188 had the highest value at −57.205 kcal/mol, signifying strong stabilizing interactions, whereas CNP0007146 had the weakest at −46.352 kcal/mol. Concerning covalent interaction energy, CNP0007442 likewise had the highest value at 11.771 kcal/mol, while CNP0007146 recorded the lowest at 3.640 kcal/mol. Additionally, CNP0007442 showed the highest solvation energy at 45.034 kcal/mol, with CNP0007506 having the lowest contribution from hydrogen bonding, recorded at

TABLE 1 | Molecular docking scores and potential residual interaction from COCONUT database with HisIE (HB, hydrogen bond; Pi–Pi, Pi–Pi stacking; SB, salt bridge).

S. no	Compound ID	Docking score (kcal/mol)	Glide energy (kcal/mol)	Glide emodel	Interaction residues	
					Chain A	Chain B
1	CNP0007188	−9.22	−62.95	−92.67	Val33(HB), Trp35(Pi-Pi), Lys 63(HB), His98(HB), Zn	Glu14(HB, SB), Asp83(SB)
2	CNP0007442	−9.15	−58.41	−90.13	Val33(HB), Trp35(Pi-Pi), Lys 63(HB), His98(HB), Zn	Glu14(HB, SB), Asp83(SB)
3	CNP0007145	−8.89	−59.37	−95.06	Val33(HB), Trp35(Pi-Pi), Lys 63(Pi-Cation), His98(HB), Zn	Glu14(HB, SB), Asp83(SB)
4	CNP0007506	−8.67	−54.14	−82.33	Val33(HB), Trp35(Pi-Pi), His98(HB), Zn	Glu14(HB, SB), Asp83(SB)
5	CNP0007146	−8.85	−52.82	−82.92	Val33(HB), Trp35(Pi-Pi), His98(HB), Zn	Glu14(HB, SB), Asp83(SB)

TABLE 2 | Predicted ADME properties of selected compounds.

S. no	Compound ID	QPlog Pw	QPlog Po/w	QPlogS	QPlog HERG	QPP Caco	QPP MDCK	% Human oral absorption
1	CNP0007188	14.93	4.49	−5.49	−6.33	338.43	461.68	100
2	CNP0007442	16.01	3.53	−4.64	−6.12	186.69	240.79	88.30
3	CNP0007145	15.26	4.1	−4.83	−6.48	292.49	473.50	95.08
4	CNP0007506	13.84	3.31	−4.17	−5.02	414.44	620.89	93.197
5	CNP0007146	12.19	4.78	−5.5	−7.55	611.21	1006.53	100

Note: This table presents key pharmacokinetic properties to evaluate the drug-likeness and absorption potential of the selected lead compounds.

34.935 kcal/mol. The values indicate stabilizing interactions, with CNP0007188 demonstrating the strongest hydrogen bonding at −2.398 kcal/mol. CNP0007188 had the most potent interaction for hydrophobic binding at −25.649 kcal/mol, while CNP0007442 had the weakest at −21.036 kcal/mol. In terms of overall stability, the most stable complex was CNP0007188, with a binding energy of −56.058 kcal/mol, followed by CNP0007145 at −51.332 kcal/mol, and CNP0007442 had the least stable binding energy at −45.411 kcal/mol, respectively (Table 3).

3.9 | Interaction Profiling of the Compounds

3.9.1 | Binding Mode Analysis of HisIE—CNP0007188

The first-ranked compound CNP0007188, 4-hydroxy-N-(4-methoxyphenyl)-4-{2-[(1,2,3,4-tetrahydroisoquinolin-2-yl)methyl]-1,3-thiazol-4-yl} piperidine-1-carboxamide, has a high docking score of −9.229 kcal/mol, a Glide emodel of −92.671 kcal/mol, and a Glide energy of −62.958 kcal/mol. These THIQ derivatives have gained considerable attention due to their well-established antibacterial potential [52]. The carboxyl group of Val33 in monomer A forms a hydrogen bond with the hydroxyl group of the ligand at a distance of 1.97 Å. The amine groups in Lys63 and His98 in monomer A interact with the carboxyl group of the ligand and contribute to the formation of hydrogen bonds at distances of 2.76 Å and 1.81 Å, respectively. Additionally, the carboxyl group of Glu14 from monomer B forms a hydrogen bond with the ligand's amine group at a distance of 1.86 Å. Additionally, π–π interactions involving Trp35 of monomer A and the formation of a salt bridge between Glu14 and Asp83 of monomer B were observed. Also, Zn^{2+} forms two metal coordinates with the N and OH groups of the ligand at distances of 2.32 Å and 1.16 Å. The key interaction residues, such as Val33, Lys63, and His98 from monomer A and Glu14 from monomer B, form stable hydrogen bond interactions. The hydroxy group of the ligand coordinates with Zn^{2+} at a distance of

TABLE 3 | MMGBSA analysis of the top lead compounds.

S. no	Compound ID	ΔG coulomb (kcal/mol)	ΔG Vdw (kcal/mol)	ΔG covalent (kcal/mol)	ΔG solv (kcal/mol)	ΔG hbond (kcal/mol)	ΔG bindlipo (kcal/mol)	ΔG bind (kcal/mol)
1	CNP0007188	−19.887	−57.204	8.464	43.748	−2.398	−56.058	−42.441
2	CNP0007442	−23.796	−50.481	11.771	45.034	−2.388	−45.410	−56.420
3	CNP0007145	−20.815	−49.188	6.810	42.473	−2.127	−51.332	−36.020
4	CNP0007506	−15.237	−49.976	8.149	34.934	−2.042	−51.036	−49.593
5	CNP0007146	−14.185	−46.352	3.640	38.718	−1.545	−49.593	−22.499

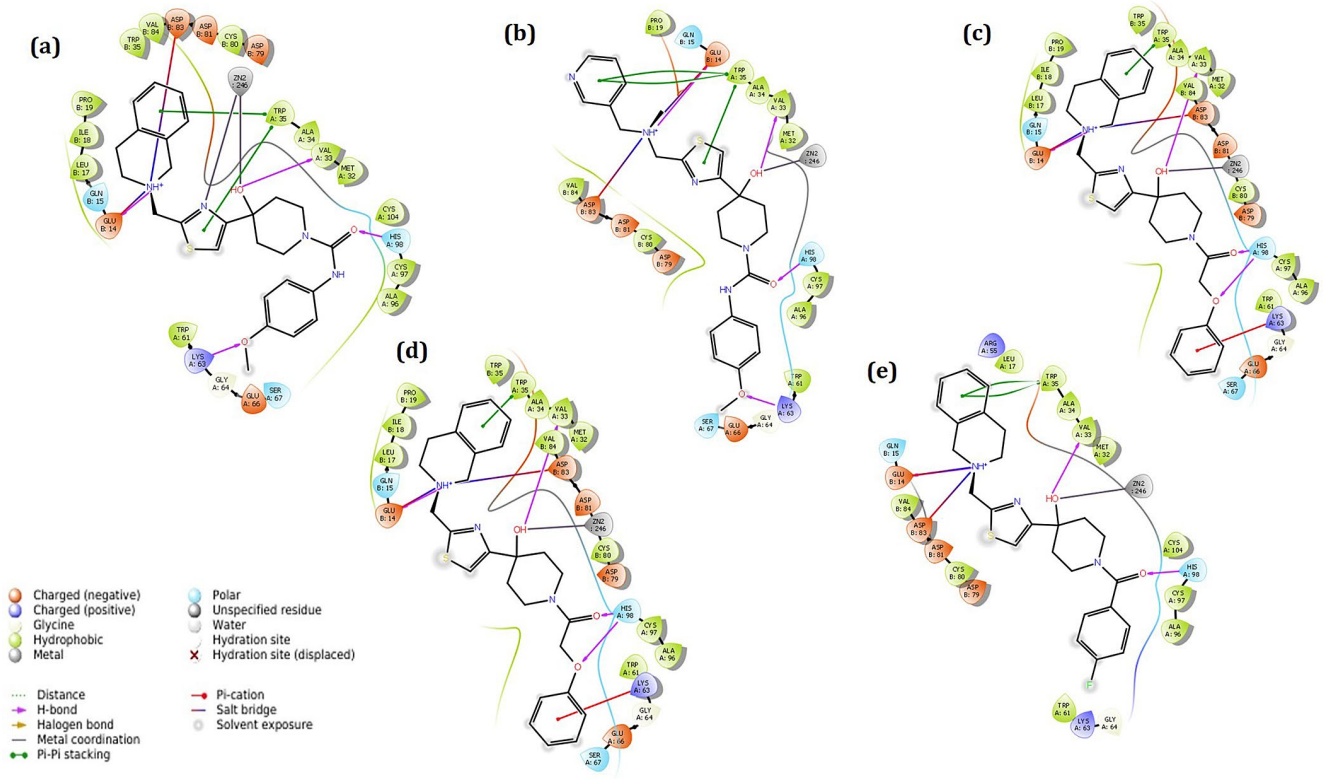

FIGURE 7 | 2D interaction profile of *Ab*HisIE docked complex (a) CNP0007188 (b) CNP0007442 (c) CNP0007145 (d) CNP0007506 (e) CNP0007146.

2.17 Å (Figure 7a and Figure S5a). Along with contributions from non-polar and charged amino acids, these interactions enhance the stability of the complex, making it sufficiently potent to inhibit the target protein HisIE.

3.9.2 | Binding Mode Analysis of HisIE—CNP0007442

The second-ranked compound CNP0007442, termed as 4-hydroxy-N-(4-methoxyphenyl)-4-{2-[(1,2,3,4-tetrahydroisoquinolin-2-yl)methyl]-1,3-thiazol-4-yl}piperidine-1-carboxamide, has a docking score of −9.157 kcal/mol, a Glide emodel of −90.137 kcal/mol, and a Glide energy of −58.410 kcal/mol. In monomer A, the carboxyl group of Val33 interacts through a hydrogen bond with the ligand's hydroxyl group at a distance of 2.09 Å. These isoquinoline alkaloids have diverse and potent therapeutic potential for the development of novel isoquinoline-based antimicrobial agents [53]. Two more hydrogen bond interactions were observed between the amine group of Lys63 and His98 in monomer A and the carboxyl group of the ligand at distances of 2.69 Å and 1.96 Å. In monomer B, the carboxyl group of Glu14 binds with the amine group of the ligand at a distance of 2.01 Å. Other interactions, such as π–π stacking and salt bridges with Trp35 from monomer A and Glu14 and Asp83 from monomer B, confirm the stability of the HisIE-CNP0007442 interaction (Figure 7b and Figure S5b).

3.9.3 | Binding Mode Analysis of HisIE—CNP0007145

The compound CNP0007145 has a docking score of −8.898 kcal/mol, a Glide emodel of −95.068 kcal/mol, and a Glide energy of −59.376 kcal mol^{-1} termed as 1-(4-hydroxy-4-{2[(1,2,3,4tetrahydroisoquinolin-2-yl) methyl]-1,3-thiazol-4-yl} piperidin-1-yl)-2-phenoxyethan-1-one. The remarkable therapeutic versatility of the isoquinoline scaffold in these alkaloids presents a remarkable antimicrobial property [53]. At a distance of 1.75 Å and 2.72 Å, two hydrogen bonds were formed between the amine group of His98 from monomer A and the carboxyl group of the ligand. Additionally, the carboxyl group of Val33 interacts through hydrogen bonds at a distance of 1.99 Å in the same chain as the ligand's hydroxyl group. The carboxyl group of Glu14 from another monomer forms a hydrogen bond and salt bridge at a distance of 1.86 Å and 4.91 Å with the amide group of the ligand. π–π and π–cation interactions were also observed in Trp35 and Lys63 from monomer A (Figure 7c and Figure S5c). Two salt bridges exist in Glu14 and Asp83 in Monomer B.

3.9.4 | Binding Mode Analysis of HisIE—CNP0007506

The docked complex of HisIE with compound 1-(morpholine-4-carbonyl)-4-{2-[(1,2,3,4-tetrahydroisoquinolin-2-yl)methyl]-1,3-thiazol-4-yl}piperidin-4-ol (compound ID: CNP0007506) has a docking score of −8.670 kcal/mol, Glide emodel of −82.338 kcal/mol, and Glide energy of −54.144 kcal/mol. This compound is a derivative of the organic tetrahydroisoquinoline (THIQ) class and has been evaluated for its antimicrobial activity [54]. Two hydrogen bonds exist between the carboxyl group of Val33 and Glu14 from monomers A and B, which bind with the hydroxyl and amine groups of the ligand at distances of 2.22 Å and 1.64 Å, respectively. One more formation of stable hydrogen bonds was observed at a distance of 2.39 Å between the amine and carboxyl group of His98 and the ligand. There were two π–π interactions in the Trp35 monomer A at distances of 5.47 and 4.18 Å. Also, two salt bridges were observed between the Glu14 and Asp83 carboxyl group from monomer B and the amine group of the ligand at distances of 4.75 and 4.26 Å. Metal coordination was observed with the Zn^{2+} and hydroxyl group of the ligand at a distance of 2.04 Å (Figure 7d and Figure S5d).

3.9.5 | Binding Mode Analysis of HisIE—CNP0007146

The compound ID: CNP0007146, termed as (1-(4-fluoro benzoyl)-4-{2-[(1,2,3,4-tetrahydroisoquinolin-2-yl)methyl]-1,3-thiazol-4-yl}piperidin-4-ol), docked with the target protein HisIE with a score of −8.859 kcal/mol, Glide emodel of −82.926 kcal/mol, and Glide energy of −52.828 kcal/mol. This organic compound belongs to a class of tetrahydroisoquinoline (THIQ) that possesses significant antibacterial activity [54]. Two hydrogen-stable bonds were observed at the distances of 1.91 and 2.52 Å with the carboxyl group of Val33 and amine group of His98 of monomer A toward the hydroxyl group of the ligand. In monomer A, two π–π stacking interactions were noticed with Trp35 at the distances of 4.53 Å and 3.92 Å. A total of two salt bridges were observed in monomer B, Glu14, and Asp83 at distances of 4.80 Å and 4.09 Å. Zn^{2+} and the ligand hydroxy group exhibited metal coordination at a distance of 2.23 Å (Figure 7e and Figure S5e).

3.10 | Frontier Molecular Orbital (FMO) Analysis

Figure 8 and Table 4 provide comprehensive insights into the electronic characteristics of the top five compounds (CNP0007188, CNP0007442, CNP0007145, CNP0007506, and CNP0007146). These characteristics are evaluated through the analysis of HOMO, LUMO, and the energy gap. The HOMO values range from −0.2035 eV to −0.2443 eV, with CNP0007146 exhibiting the most negative HOMO value of −0.2443 eV, indicating the highest stability of its occupied orbitals. The LUMO values vary from −0.0570 eV to −0.0583 eV, with CNP0007145 demonstrating the lowest negative LUMO value at −0.0570 eV, suggesting a stronger propensity for electron acceptance. The energy gap, which represents the difference between HOMO and LUMO, ranges from −0.1449 eV to −0.1861 eV. Notably, CNP0007442 has the smallest energy gap of −0.1449 eV, indicating enhanced conductivity and reduced excitation energy, making it more reactive. In contrast, CNP0007188, CNP0007145, and CNP0007506 exhibit moderate energy gap values, which suggest structural stability. CNP0007146 has the most prominent energy gap of −0.1861 eV, indicating reduced reactivity and higher stability. The data presented provide valuable insights into the compounds' reactivity, stability, and potential applications.

3.11 | Comparative MD Analysis of Dimeric HisIE and Ligand Complexes

Molecular dynamics simulation studies assessed predicted protein models' stability and dynamic behavior. Root mean square

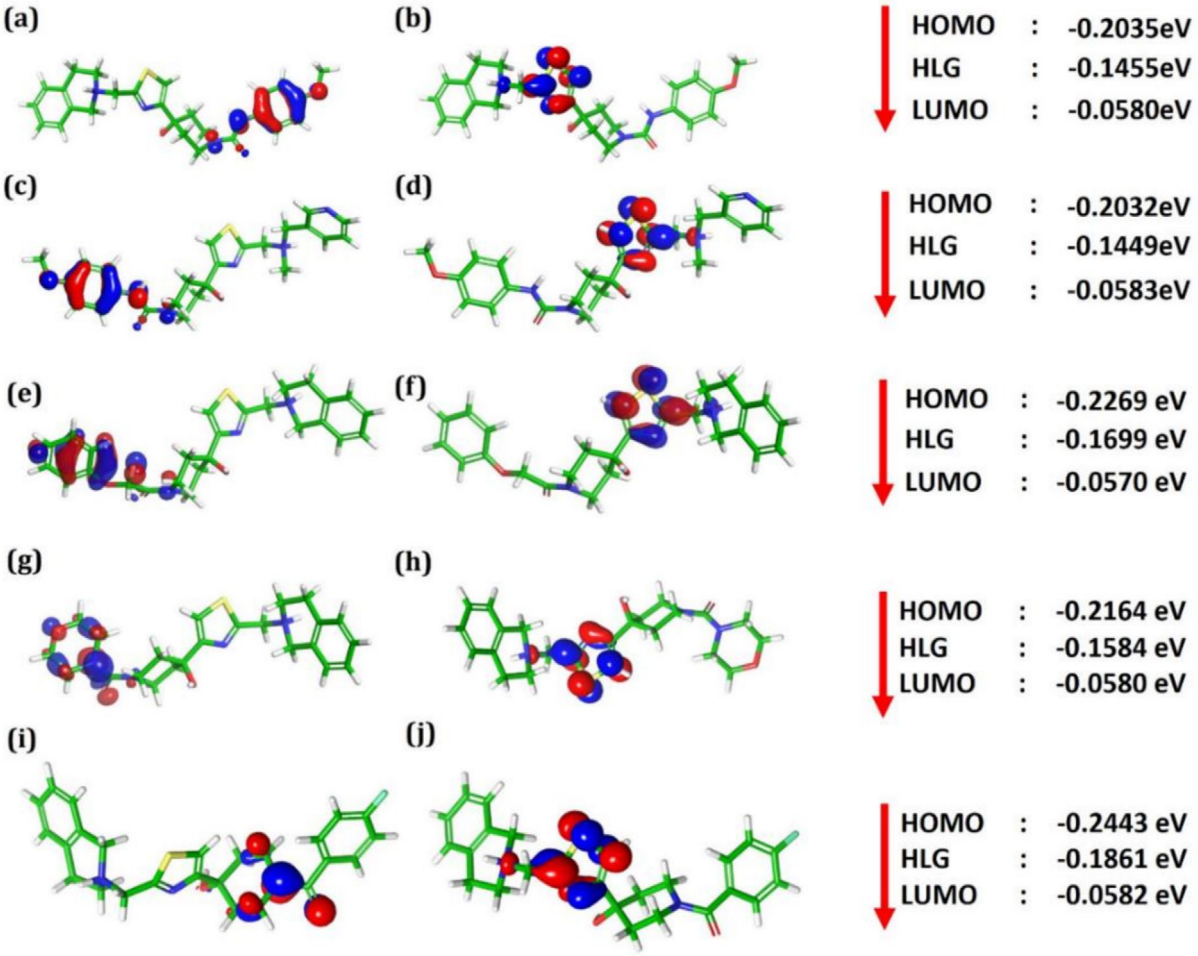

FIGURE 8 | FMO analysis of top compounds illustrates the distributions of the HOMO and LUMO, along with their corresponding energy values (eV), which highlight the electronic properties and stability of the compounds.

TABLE 4 | Frontier molecular orbital energy values of the top five compounds.

S.No	Compound ID	HOMO (eV)	LUMO (eV)	Energy gap (eV)
1	CNP0007188	−0.203	−0.058	−0.145
2	CNP0007442	−0.203	−0.058	−0.144
3	CNP0007145	−0.226	−0.057	−0.169
4	CNP0007506	−0.216	−0.058	−0.158
5	CNP0007146	−0.244	−0.058	−0.186

deviation (RMSD), which measures the average displacement of backbone atoms from the initial structure, and root mean square fluctuation (RMSF), which indicates residue flexibility, are the vital metrics of MDS. The overall stability of the protein can be determined by analyzing these metrics. RMSF provides insights into the dynamic movements of individual amino acids. Together, these offer a comprehensive view of the modeled protein's conformational stability. The RMSD values for Chain A exhibited relative consistency across all analyzed complexes, with mean values ranging from 0.448 nm to 0.815 nm and standard deviations varying from 0.071 nm to 0.328 nm. ChainA_CNP0007145 displayed the lowest mean RMSD of 0.448 nm, indicative of superior structural stability, in contrast to ChainA_CNP0007146, which recorded the highest mean RMSD of 0.815 nm, reflecting increased flexibility relative to the other complexes (Figure 9a). In comparison, Chain B showed higher RMSD values, with means ranging from 0.573 nm to 1.347 nm and standard deviations between 0.113 nm and 0.494 nm. Notably, ChainB_CNP0007146 exhibited the highest mean RMSD, while ChainB_CNP0007145 recorded the lowest mean value of 0.573 nm (Figure 9b). A comparative analysis of the RMSD profiles indicated that complexes associated with CNP0007188, CNP0007442, CNP0007145, and CNP0007506 maintained structural stability, whereas CNP0007146 displayed minor variations. Nevertheless, despite these fluctuations, all protein–ligand complexes remained in equilibrium throughout the MD simulation, signifying overall stability.

From the RMSF analysis, most of the residues in Chain A remained stable, with minor deviations (Figure 9c). However, notable fluctuations were observed in the dimeric loop residues in all the complexes, with RMSF values ranging from ~0.90 nm to ~1.14 nm. Except for Protein-CNP0007146, higher fluctuations were observed in the HisE region, particularly Arg241 (0.83 nm), Arg242 (0.79 nm), Thr125 (0.78 nm), and Glu163 (0.77 nm), indicating greater flexibility. In the case of Chain B, all the complexes

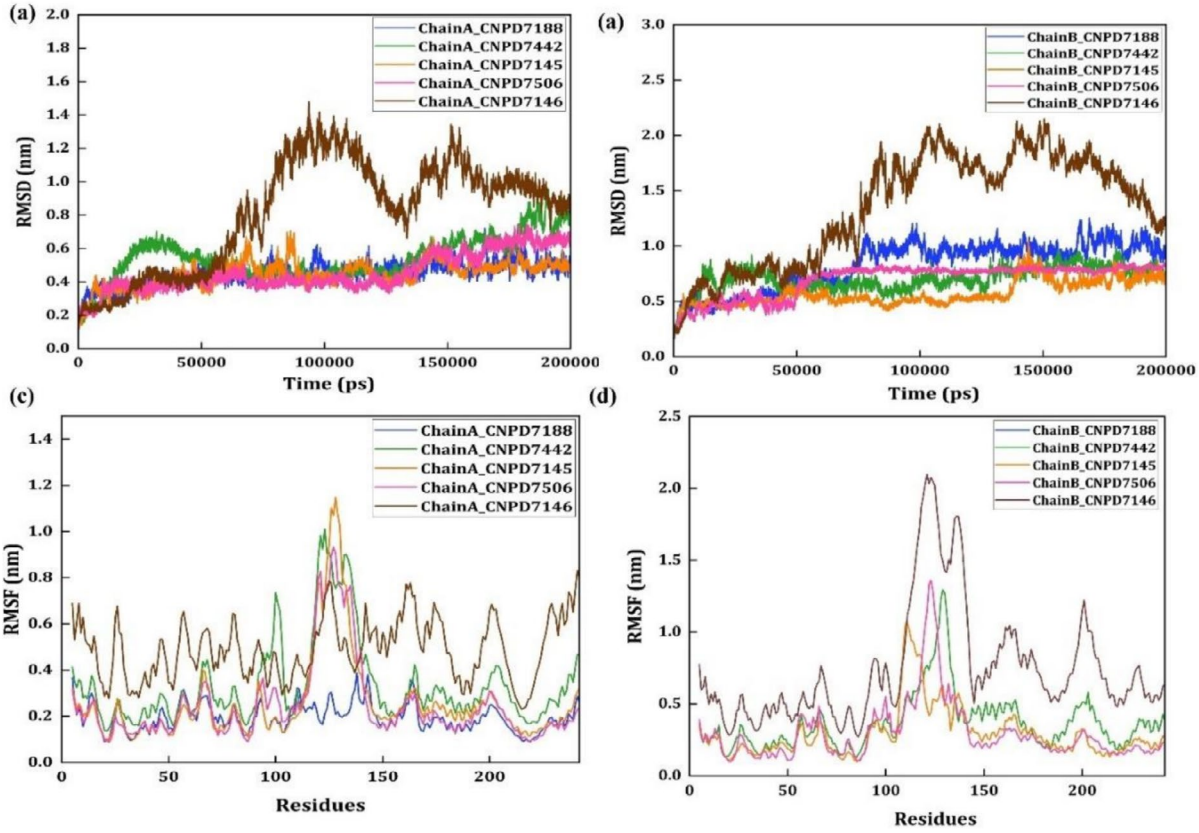

FIGURE 9 | Molecular dynamics simulation analysis of the dimeric *Ab*HisIE–inhibitor complexes (a) Comparative RMSD analysis of Chain A, (b) comparative RMSD analysis of Chain B, RMSF analysis of (c) Chain A and (d) Chain B.

have similar RMSF profiling as that of Chain A, wherein the dimeric loop residues have shown higher fluctuations around ~1.2 nm to ~1.33 nm. Regarding the Chain B RMSF analysis, HisIE in complexes with CNP0007188 and CNP0007146 compounds exhibited similar RMSF profiles. In these complexes, the dimeric loop (DL) region residues (Leu121, Lys121, Asp122, and Pro124) showed elevated fluctuations, ranging from 2.09 to 2.03 nm (Figure 9d). In contrast, CNP0007442 dimeric loop (DL) residues Tyr128, Gly129, and Asp130 demonstrated higher peaks, around 1.2 nm, indicating increased residual mobility. Crucial residues, such as Glu14 and Asp83, displayed minimal fluctuations, particularly in the HisI region. The highest fluctuations observed overall were the residues in the dimeric loop region, emphasizing its dynamic nature. Both CNP0007145 and CNP0007506 exhibited fluctuation peaks reaching up to 1.06 nm in the HisI region residues, namely, Thr110, Pro111, and Gly112. Additionally, a peak of 1.33 nm in CNP0007506 was observed in the dimeric loop residues Leu121, Lys121, Asp122, and Pro124. Most residues in the dimerization loop presented distinct peaks in both chains. Overall, Chain A complexes exhibited lower fluctuations than Chain B, which infers that Chain A has dramatically aided in the increased stability of the complexes. The Radius of Gyration analysis across two chains, Chain A and Chain B, over various simulation periods shows that the mean Rg values for Chain B are generally higher than those for Chain A (Figure 10a). Specifically, CNP0007146 exhibits the highest mean value in both chains, particularly in Chain B, indicating a potentially significant deviation or fluctuation for this compound (Figure 10b). This suggests differences in the compactness of the compounds in the two chains. The comparative analysis of hydrogen bonds revealed that CNP0007506 formed the most substantial interactions, consistently maintaining five hydrogen bonds (Figure 10c). In contrast, CNP0007146 maintained four hydrogen bonds throughout the simulation, while CNP0007188, CNP0007442, and CNP0007145 demonstrated stable interactions with three hydrogen bonds each. In the case of H-bond interactions with Chain B residues, it was inferred that, on average, only two hydrogen bonds are maintained throughout the MD run in all the complexes (Figure 10d). From the structural superimposition analysis of the initial (0^{th} ns) and the final (200^{th} ns) conformation of the complexes, it was inferred that the loop segment (His98-Gly129) spans the dimeric loop of Chain A, and the loop segment (Gln5-Leu17) spans the HisI domain of Chain B, which underwent noticeable displacement upon ligand binding across all complexes. This observation suggests that the inhibitors have the potential to modulate local structural flexibility and influence the overall protein dynamics. The root mean square deviation (RMSD) values between the simulated structures at 0^{th} ns and 200^{th} ns for the five protein–compound complexes were observed as 6.061, 6.525, 4.748, 4.442, and 7.971 Å, respectively (Figures S6 and S7).

3.12 | MMPBSA Analysis

The MMPBSA analysis for the top five lead compounds (CNP0007442, CNP0007188, CNP0007146, CNP0007506, and CNP0007145) shows considerable variations in binding energies

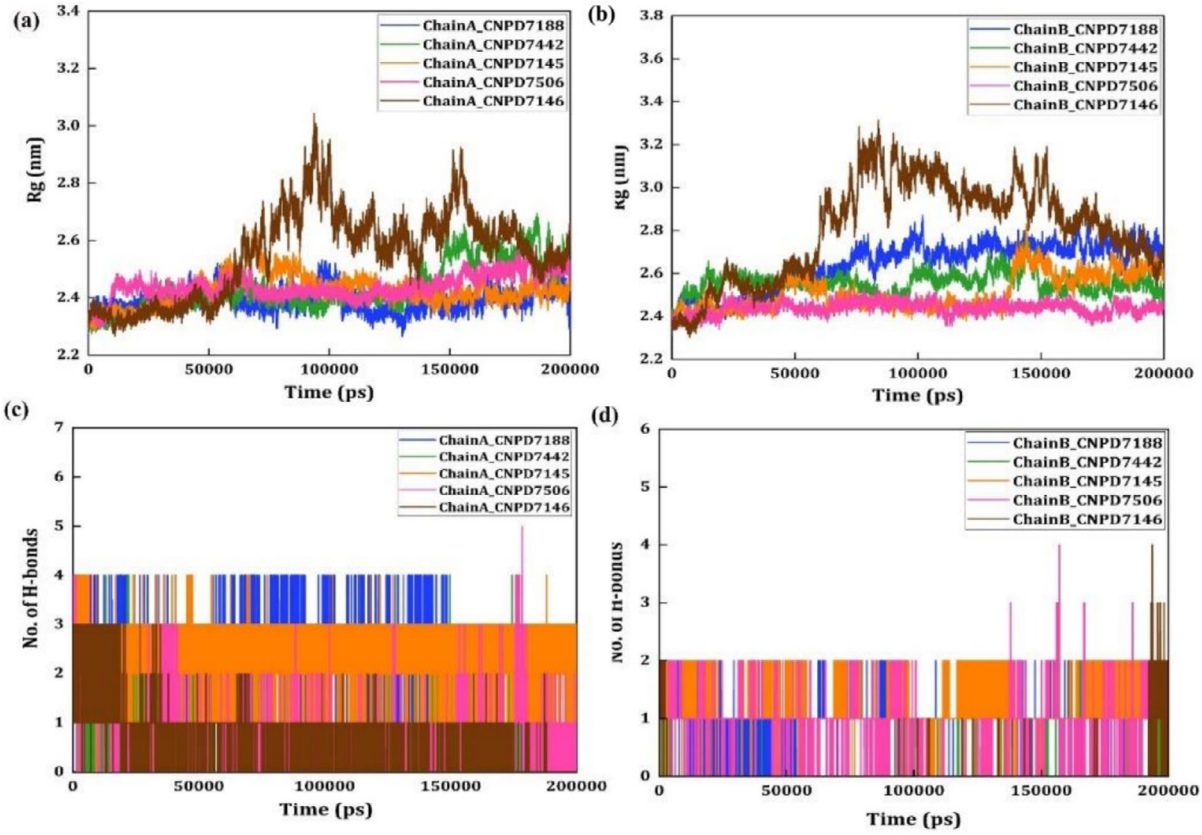

FIGURE 10 | Comparative radius of gyration analysis of dimeric *Ab*HisIE-inhibitor complexes (a) Chain A, (b) Chain B, comparative H-bond analysis of identified compounds with (c) Chain A and (d) Chain B of dimeric AbHisIE-inhibitor complexes.

(Figure S8). All the lead compounds exhibit favorable binding affinities, indicated by their negative total binding free energies (TOTAL). CNP0007442 (−21.81 kcal/mol) and CNP0007145 (−20.93 kcal/mol) demonstrate the most substantial binding. These compounds benefit from favorable Van der Waals (VDWAALS) and electrostatic (EEL) interactions. However, these advantages are relatively offset by unfavorable polar solvation energies (EGB) caused by polar group desolvation. Both CNP0007188 (−20.09 kcal/mol) and CNP0007506 (−15.45 kcal/mol) show good binding as well, but they have significantly weaker electrostatic interactions and minor desolvation penalties compared with the top two compounds. In contrast, CNP0007146 has the lowest binding affinity (−2.61 kcal/mol) due to less favorable Van der Waals, electrostatic interactions, and a more significant polar solvation penalty. On the other hand, the substrate has a very unfavorable binding free energy of 198.5 kcal/mol. This poor binding is primarily due to strong repulsive electrostatic interactions (EEL = 847.23 kcal/mol) and a highly favorable polar solvation energy (EGB = −612.51 kcal/mol). Overall, the lead compounds tend to strike a balance between strong gas-phase interactions and solvation penalties, with CNP0007442 and CNP0007145 emerging as the most promising candidates due to their lower overall binding energies.

To advance these two promising compounds toward drug development, further lead optimization is needed to enhance their safety, stability, and effectiveness. This includes refining their chemical structure to improve how well they are absorbed and distributed in the body, reducing potential side effects. Minor adjustments to the molecules may also help improve their binding to the target enzyme and make them more selective, reducing the risk of affecting nontarget proteins. Additionally, improving their metabolic stability could ensure they remain active in the body for a sufficient period. These steps are essential before moving to laboratory testing and eventual clinical evaluation.

4 | Conclusion

This study targets *A. baumannii* HisIE (*Ab*HisIE), a key enzyme in histidine biosynthesis, to identify potential antimicrobial inhibitors. A dimeric *Ab*HisIE model was constructed using homology modeling, and its stability was analyzed through molecular dynamics (MD) simulations. Docking studies confirmed strong substrate binding, with Chain B exhibiting higher compactness and stability. High-throughput virtual screening identified CNP0007188, CNP0007442, and CNP0007145 as promising inhibitors based on docking scores, hydrogen bonding, and Zn^{2+} coordination. ADME/T analysis confirmed their drug-like properties, while MM/GBSA analysis highlighted CNP0007188 as the most stable complex. MD simulations revealed that Chain A remained stable, whereas Chain B showed fluctuations in the dimerization loop. RMSD and hydrogen bond analyses further supported CNP0007442 and CNP0007145 as strong and stable binders. Overall, CNP0007442 and CNP0007145 emerged as the most promising inhibitors of *Ab*HisIE, demonstrating strong interactions and stability. These findings provide valuable insights for developing novel therapeutics against *A. baumannii*;

however, they warrant further lead optimization and experimental validations.

Acknowledgments

R.R. acknowledges the Indian Council of Medical Research, New Delhi (ICMR), for providing financial assistance through ICMR/SRF Fellowship (AMR/Fellowship/24/2022-ECD-II). N.H. greatly acknowledges the Department of Science and Technology (DST) for financial assistance through DST/INSPIRE Fellowship/2019/IF190083. J.J. thanks the Department of Biotechnology (DBT)-Bioinformatics Centre: (Grant No. [BIC]-No.BT/PR40154/BTIS/137/34/2021), Ministry of Human Resource Development—Rashtriya Uchchatar Shiksha Abhiyan (MHRD-RUSA 2.0): (Grant No. F.24e51/2014-U, Policy [TNMulti-Gen]), Department of Biotechnology—National Network Project (DBT-NNP) (Grant No. BT/PR40156/BTIS/137/54/2023), and the Indian Council of Medical Research, New Delhi Women Scientist Fellowship (R.12013/30/2024-HR).

Conflicts of Interest

The authors declare no conflicts of interest.

Data Availability Statement

The data that support the findings of this study are available from the corresponding author upon reasonable request.

References

1. A. Fiser and A. Šali, "Modeller: Generation and Refinement of Homology-Based Protein Structure Models," *Methods in Enzymology* 374 (2003): 461–491.

2. H. W. Boucher, G. H. Talbot, J. S. Bradley, et al., "Bad Bugs, No Drugs: No ESKAPE! An Update From the Infectious Diseases Society of America," *Clinical Infectious Diseases* 48, no. 1 (2009): 1–12.

3. D. Wong, T. B. Nielsen, R. A. Bonomo, P. Pantapalangkoor, B. Luna, and B. Spellberg, "Clinical and Pathophysiological Overview of Acinetobacter Infections: A Century of Challenges," *Clinical Microbiology Reviews* 30, no. 1 (2017): 409–447.

4. J. N. Pendleton, S. P. Gorman, and B. F. Gilmore, "Clinical Relevance of the ESKAPE Pathogens," *Expert Review of Anti-Infective Therapy* 11, no. 3 (2013): 297–308.

5. N. Puvača, J. Milenković, T. Galonja Coghill, et al., "Antimicrobial Activity of Selected Essential Oils Against Selected Pathogenic Bacteria: In Vitro Study," *Antibiotics* 10, no. 5 (2021): 546.

6. C. Dexter, G. L. Murray, I. T. Paulsen, and A. Y. Peleg, "Community-Acquired *Acinetobacter baumannii*: Clinical Characteristics, Epidemiology and Pathogenesis," *Expert Review of Anti-Infective Therapy* 13, no. 5 (2015): 567–573.

7. Z. M. Djordjevic, M. M. Folic, N. D. Folic, N. Gajovic, O. Gajovic, and S. M. Jankovic, "Risk Factors for Hospital Infections Caused by Carbapanem-Resistant *Acinetobacter baumannii*," *Journal of Infection in Developing Countries* 10, no. 10 (2016): 1073–1080.

8. H.-Y. Lee, S.-Y. Hsu, J.-F. Hsu, C. L. Chen, Y. H. Wang, and C. H. Chiu, "Risk Factors and Molecular Epidemiology of *Acinetobacter baumannii* Bacteremia in Neonates," *Journal of Microbiology, Immunology and Infection* 51, no. 3 (2018): 367–376.

9. E.-T. Piperaki, L. S. Tzouvelekis, V. Miriagou, and G. L. Daikos, "Carbapenem-Resistant *Acinetobacter baumannii*: In Pursuit of an Effective Treatment," *Clinical Microbiology and Infection* 25, no. 8 (2019): 951–957.

10. S. E. Weinberg, A. Villedieu, N. Bagdasarian, N. Karah, L. Teare, and W. F. Elamin, "Control and Management of Multidrug Resistant *Acinetobacter baumannii*: A Review of the Evidence and Proposal of Novel Approaches," *Infection Prevention in Practice* 2, no. 3 (2020): 100077.

11. M. I. El-Gamal, I. Brahim, N. Hisham, et al., "Recent Updates of Carbapenem Antibiotics," *European Journal of Medicinal Chemistry* 131 (2017): 185–195.

12. C. Müller, S. Reuter, J. Wille, et al., "A Global View on Carbapenem-Resistant *Acinetobacter baumannii*," *MBio* 14, no. 6 (2023): e02260-23.

13. K. M. Papp-Wallace, A. Endimiani, M. A. Taracila, and R. A. Bonomo, "Carbapenems: Past, Present, and Future," *Antimicrobial Agents and Chemotherapy* 55, no. 11 (2011): 4943–4960.

14. E. Tacconelli, E. Carrara, A. Savoldi, et al., "Discovery, Research, and Development of New Antibiotics: The WHO Priority List of Antibiotic-Resistant Bacteria and Tuberculosis," *Lancet Infectious Diseases* 18, no. 3 (2018): 318–327.

15. V. Tiku, "*Acinetobacter baumannii*: Virulence Strategies and Host Defense Mechanisms," *DNA and Cell Biology* 41, no. 1 (2022): 43–48.

16. M. Serra-Burriel, M. Keys, C. Campillo-Artero, et al., "Impact of Multi-Drug Resistant Bacteria on Economic and Clinical Outcomes of Healthcare-Associated Infections in Adults: Systematic Review and Meta-Analysis," *PLoS One* 15, no. 1 (2020): e0227139.

17. B. J. Langford, M. So, M. Simeonova, et al., "Antimicrobial Resistance in Patients With COVID-19: A Systematic Review and Meta-Analysis," *Lancet Microbe* 4, no. 3 (2023): e179–e191, https://doi.org/10.1016/S2666-5247(22)00355-X. Epub 2023 Jan 31.

18. J. Li, J. Wang, Y. Yang, et al., "Etiology and Antimicrobial Resistance of Secondary Bacterial Infections in Patients Hospitalized With COVID-19 in Wuhan, China: A Retrospective Analysis," *Antimicrobial Resistance and Infection Control* 9, no. 1 (2020): 153.

19. R. Mirzaei, P. Goodarzi, M. Asadi, et al., "Bacterial Co-Infections With SARS-CoV-2," *IUBMB Life* 72, no. 10 (2020): 2097–2111.

20. C. H. Rodríguez, N. Balderrama Yarhui, M. Nastro, et al., "Molecular Epidemiology of Carbapenem-Resistant *Acinetobacter baumannii* in South America," *Journal of Medical Microbiology* 65, no. 10 (2016): 1088–1091.

21. É. Ruppé, P.-L. Woerther, and F. Barbier, "Mechanisms of Antimicrobial Resistance in Gram-Negative Bacilli," *Annals of Intensive Care* 5, no. 1 (2015): 21.

22. Z. A. Qureshi, L. E. Hittle, J. A. O'Hara, et al., "Colistin-Resistant *Acinetobacter baumannii*: Beyond Carbapenem Resistance," *Clinical Infectious Diseases* 60, no. 9 (2015): 1295–1303.

23. M. E. Winkler and S. Ramos-Montañez, "Biosynthesis of Histidine," *EcoSal Plus* 3, no. 2 (2009), https://doi.org/10.1128/ecosalplus.3.6.1.9.

24. R. Fani, M. Brilli, M. Fondi, and P. Lió, "The Role of Gene Fusions in the Evolution of Metabolic Pathways: The Histidine Biosynthesis Case," *BMC Evolutionary Biology* 7, no. Suppl 2 (2007): S4.

25. K. Conde-Pérez, J. C. Vázquez-Ucha, L. Álvarez-Fraga, et al., "In-Depth Analysis of the Role of the Acinetobactin Cluster in the Virulence of *Acinetobacter baumannii*," *Frontiers in Microbiology* 12 (2021): 752070.

26. Z. R. Lonergan, L. D. Palmer, and E. P. Skaar, "Histidine Utilization Is a Critical Determinant of *Acinetobacter* Pathogenesis," *Infection and Immunity* 88, no. 7 (2020): e00118-20.

27. N. Wang, E. A. Ozer, M. J. Mandel, et al., "Genome-Wide Identification of *Acinetobacter baumannii* Genes Necessary for Persistence in the Lung," *MBio* 5, no. 3 (2014): e01163-14.

28. M. Brilli and R. Fani, "The Origin and Evolution of Eucaryal HIS7 Genes: From Metabolon to Bifunctional Proteins?," *Gene* 339 (2004): 149–160.

29. M. Brilli and R. Fani, "Molecular Evolution of HisB Genes," *Journal of Molecular Evolution* 58, no. 2 (2004): 225–237.

30. S. T. Henriksen, J. Liu, G. Estiu, Z. N. Oltvai, and O. Wiest, "Identification of Novel Bacterial Histidine Biosynthesis Inhibitors Using Docking, Ensemble Rescoring, and Whole-Cell Assays," *Bioorganic & Medicinal Chemistry* 18, no. 14 (2010): 5148–5156.

31. D.-S. Lee, H. Burd, J. Liu, et al., "Comparative Genome-Scale Metabolic Reconstruction and Flux Balance Analysis of Multiple *Staphylococcus aureus* Genomes Identify Novel Antimicrobial Drug Targets," *Journal of Bacteriology* 191, no. 12 (2009): 4015–4024.

32. Y. Shen, J. Liu, G. Estiu, et al., "Blueprint for Antimicrobial Hit Discovery Targeting Metabolic Networks," *Proceedings of the National Academy of Sciences of the United States of America* 107, no. 3 (2010): 1082–1087.

33. R. Rajmichael, N. Hemavathy, A. Mathimaran, et al., "Whole Genome Sequencing Characterization and Comparative Genome Analysis of *Acinetobacter baumannii* JJAB01: A Comprehensive Insights on Antimicrobial Resistance and Virulence Genotype," *Microbial Pathogenesis* 199 (2025): 107224.

34. J. M. Walker, ed., *The Proteomics Protocols Handbook* (Humana Press, 2005), https://doi.org/10.1385/1592598900.

35. C. Geourjon and G. Deléage, "SOPMA: Significant Improvements in Protein Secondary Structure Prediction by Consensus Prediction From Multiple Alignments," *Bioinformatics* 11, no. 6 (1995): 681–684.

36. M. Johnson, I. Zaretskaya, Y. Raytselis, Y. Merezhuk, S. McGinnis, and T. L. Madden, "NCBI BLAST: A Better Web Interface," *Nucleic Acids Research* 36, no. Web Server (2008): W5–W9.

37. R. A. Laskowski, M. W. MacArthur, D. S. Moss, and J. M. Thornton, "PROCHECK: A Program to Check the Stereochemical Quality of Protein Structures," *Journal of Applied Crystallography* 26, no. 2 (1993): 283–291.

38. M. Wiederstein and M. J. Sippl, "ProSA-Web: Interactive Web Service for the Recognition of Errors in Three-Dimensional Structures of Proteins," *Nucleic Acids Research* 35, no. Web Server (2007): W407–W410.

39. W. Yu, X. He, K. Vanommeslaeghe, and A. D. MacKerell, Jr., "Extension of the CHARMM General Force Field to Sulfonyl-Containing Compounds and Its Utility in Biomolecular Simulations," *Journal of Computational Chemistry* 33, no. 31 (2012): 2451–2468.

40. N. Hemavathy, V. Umashankar, and J. Jeyakanthan, "Unveiling Novel Type 1 Inhibitors for Targeting LIM Kinase 2 (LIMK2) for Cancer Therapeutics: An Integrative Pharmacoinformatics Approach," *Computational Biology and Chemistry* 115 (2025): 108289.

41. Y. Hirano, N. Okimoto, S. Fujita, and M. Taiji, "Molecular Dynamics Study of Conformational Changes of Tankyrase 2 Binding Subsites Upon Ligand Binding," *ACS Omega* 6, no. 27 (2021): 17609–17620.

42. R. L. D'Ordine, R. S. Linger, C. J. Thai, and V. J. Davisson, "Catalytic Zinc Site and Mechanism of the Metalloenzyme PR-AMP Cyclohydrolase," *Biochemistry* 51, no. 29 (2012): 5791–5803.

43. J. Sivaraman, R. S. Myers, L. Boju, et al., "Crystal Structure of *Methanobacterium thermoautotrophicum* Phosphoribosyl-AMP Cyclohydrolase HisI," *Biochemistry* 44, no. 30 (2005): 10071–10080.

44. J. D. Thompson, T. J. Gibson, and D. G. Higgins, "Multiple Sequence Alignment Using ClustalW and ClustalX," *Current Protocols in Bioinformatics* Chapter 2 (2003): Unit 2.3.

45. Y. Wang, F. Zhang, Y. Nie, G. Shang, and H. Zhang, "Structural Analysis of *Shigella flexneri* Bi-Functional Enzyme HisIE in Histidine Biosynthesis," *Biochemical and Biophysical Research Communications* 516, no. 2 (2019): 540–545.

46. R. A. Friesner, J. L. Banks, R. B. Murphy, et al., "Glide: A New Approach for Rapid, Accurate Docking and Scoring. 1. Method and Assessment of Docking Accuracy," *Journal of Medicinal Chemistry* 47, no. 7 (2004): 1739–1749.

47. N. Sharma, L. D. Naorem, S. Jain, and G. P. S. Raghava, "ToxinPred2: An Improved Method for Predicting Toxicity of Proteins," *Briefings in Bioinformatics* 23, no. 5 (2022): bbac174.

48. S. Subramaniyan, H. Nagarajan, U. Vetrivel, and J. Jeyaraman, "Multilayer Precision-Based Screening of Potential Inhibitors Targeting *Mycobacterium tuberculosis* Acetate Kinase Using In Silico Approaches," *Computational Biology and Chemistry* 107 (2023): 107942.

49. A. D. Bochevarov, E. Harder, T. F. Hughes, et al., "Jaguar: A High-Performance Quantum Chemistry Software Program With Strengths in Life and Materials Sciences," *International Journal of Quantum Chemistry* 113, no. 18 (2013): 2110–2142.

50. P. Sangavi, H. Nagarajan, S. Subramaniyan, S. Jeyaraman, and K. Langeswaran"Unveiling the Oncological Inhibition of Bioactive Compounds From *Adansonia digitata* via *In Silico* Analysis by Targeting γ-Butyrobetaine Dioxygenase 1 Against Triple Negative Breast Cancer," *Journal of Biomolecular Structure and Dynamics* (2024): 1–24, https://doi.org/10.1080/07391102.2024.2437528.

51. M. S. Valdés-Tresanco, M. E. Valdés-Tresanco, P. A. Valiente, and E. Moreno, "gmx_MMPBSA: A New Tool to Perform End-State Free Energy Calculations With GROMACS," *Journal of Chemical Theory and Computation* 17, no. 10 (2021): 6281–6291.

52. G.-L. Tang, M.-C. Tang, L.-Q. Song, and Y. Zhang, "Biosynthesis of Tetrahydroisoquinoline Antibiotics," *Current Topics in Medicinal Chemistry* 16, no. 15 (2016): 1717–1726.

53. A. Galán, L. Moreno, J. Párraga, et al., "Novel Isoquinoline Derivatives as Antimicrobial Agents," *Bioorganic & Medicinal Chemistry* 21, no. 11 (2013): 3221–3230.

54. R. Tiwari, D. Singh, J. Singh, et al., "Synthesis, Antibacterial Activity and QSAR Studies of 1,2-Disubstituted-6,7-Dimethoxy-1,2,3,4-Tetra hydroisoquinolines," *European Journal of Medicinal Chemistry* 41, no. 1 (2006): 40–49.

Supporting Information

Additional supporting information can be found online in the Supporting Information section. **Figure S1:** SOPMA secondary structure prediction of *A. baumannii* HisIE (NCBI accession ID: WP_001066569.1), showing the distribution of structural composition such as helix (40.47%), strand (12.45%) and coil (47.08%). **Figure S2:** Ramachandran Plot Analysis of the Modeled Protein Structure using PROCHECK, illustrating the distribution of φ and ψ dihedral angles of amino acid residues of *Ab*HisIE (NCBI accession ID: WP_001066569.1) modeled protein structure. **Figure S3:** Structural superimposition of the predicted *Ab*HisIE model (green) with the template structure 6J2L (Brown). The root mean square deviation (RMSD) of 0.15 Å, indicating high structural similarity. Mg^{2+} and Zn^{2+} metal ions were shown in spheres. **Figure S4:** Multiple Sequence Alignment of *A. baumannii* HisIE (NCBI accession ID: WP_001066569.1), PDB ID: 1ZPS, from *Methanobacterium thermoautotrophicum*—HisI domain and PDB ID: 6J2L—from *Shigella flexneri*—HisIE, the conserved residues are highlighted in red. **Figure S5:** 3D interaction profile of *Ab*HisIE docked complex with Zn^{2+} ions (shown as magenta sphere) (a) CNP0007188 (b) CNP0007442 (c) CNP0007145 (d) CNP0007506 (e) CNP0007146. **Figure S6:** Represents the structural superimposition of the initial (0th ns) (shown in marine blue color) and final conformation (200th ns) of the HisIE–inhibitor complexes (a) HisIE- CNP0007188 complex (final conformation shown in pale green color), (b) HisIE–CNP0007442 complex (final conformation shown in pale yellow color), (c) HisIE-CNP0007145 complex (final conformation shown in pale pink color); with Zn^{2+} ions and Mg^{2+} ion was shown as orange color sphere and the inset figure represents the zoomed in orientation of the ligand at the

cavity devoid of the ions. **Figure S7:** Represents the structural superimposition of the initial (0th ns) (shown in marine blue color) and final conformation (200th ns) of the HisIE–inhibitor complexes (a) HisIE–CNP0007506 complex (final conformation shown in pale cyan color), (b) HisIE–CNP0007146 complex (final conformation shown in dark salmon color); with Zn^{2+} ions and Mg^{2+} ion was shown as orange color sphere and the inset figure represents the zoomed in orientation of the ligand at the cavity devoid of the ions. **Figure S8:** MM/PBSA analysis of the Top compounds with their decomposition energy components.